


# PHOTONICS Research

## Reliable intracavity reflection for self-injection locking lasers and microcomb generation

BITAO SHEN,<sup>1</sup> XUGUANG ZHANG,<sup>1</sup> YIMENG WANG,<sup>1</sup> ZIHAN TAO,<sup>1</sup> HAOWEN SHU,<sup>1,2,5</sup> HUAJIN CHANG,<sup>1</sup> WENCAN LI,<sup>1</sup> YAN ZHOU,<sup>3</sup>  ZHANGFENG GE,<sup>3</sup> RUIXUAN CHEN,<sup>1</sup> BOWEN BAI,<sup>1</sup> LIN CHANG,<sup>1,4,6</sup> AND XINGJUN WANG<sup>1,2,3,4,\*</sup>

<sup>1</sup>State Key Laboratory of Advanced Optical Communications System and Networks, School of Electronics, Peking University, Beijing 100871, China

<sup>2</sup>Peng Cheng Laboratory, Shenzhen 518055, China

<sup>3</sup>Peking University Yangtze Delta Institute of Optoelectronics, Nantong 226010, China

<sup>4</sup>Frontiers Science Center for Nano-optoelectronics, Peking University, Beijing 100871, China

<sup>5</sup>e-mail: haowenshu@pku.edu.cn

<sup>6</sup>e-mail: linchang@pku.edu.cn

\*Corresponding author: xjwang@pku.edu.cn

Received 9 November 2023; revised 25 February 2024; accepted 26 February 2024; posted 26 February 2024 (Doc. ID 511627); published 1 May 2024

Self-injection locking has emerged as a crucial technique for coherent optical sources, spanning from narrow linewidth lasers to the generation of localized microcombs. This technique involves key components, namely a laser diode and a high-quality cavity that induces narrow-band reflection back into the laser diode. However, in prior studies, the reflection mainly relied on the random intracavity Rayleigh backscattering, rendering it unpredictable and unsuitable for large-scale production and wide-band operation. In this work, we present a simple approach to achieve reliable intracavity reflection for self-injection locking to address this challenge by introducing a Sagnac loop into the cavity. This method guarantees robust reflection for every resonance within a wide operational band without compromising the quality factor or adding complexity to the fabrication process. As a proof of concept, we showcase the robust generation of narrow linewidth lasers and localized microcombs locked to different resonances within a normal-dispersion microcavity. Furthermore, the existence and generation of localized patterns in a normal-dispersion cavity with broadband forward-backward field coupling is first proved, as far as we know, both in simulation and in experiment. Our research offers a transformative approach to self-injection locking and holds great potential for large-scale production. © 2024 Chinese Laser Press

<https://doi.org/10.1364/PRJ.511627>

### 1. INTRODUCTION

Spectrally pure, or high-coherence lasers are crucial for a wide range of applications, including coherent optical communication [1,2], microwave photonics [3–5], optical atomic clock [6,7], ranging [8,9], precise sensing [10], and spectroscopy [11]. Among the various high-coherence laser schemes, self-injection locking (SIL) lasers [12,13] stand out as particularly promising due to the potential wafer-scale production [14], leveraging recent progress in ultralow-loss integrated optical circuits [15,16] and hybrid integration technology [17–20]. The core principle of self-injection locking lasers [21–23] involves directly coupling the laser cavity with an external, high-quality-factor microcavity [24]. In this configuration, the output of the hybrid laser cavity will be locked by the reflections from the external microcavity. This results in the suppression of phase

noise, or in other words, superior frequency stability. The intrinsic linewidth can be reduced to the remarkable level of just a few hertz [25]. Moreover, the unique dynamics in such hybrid cavities can facilitate the robust and turnkey generation of localized microcombs, successfully demonstrated in both anomalous [26,27] and normal-dispersion [28,29] microcavities.

The essential of self-injection locking technology is the narrow-band reflection induced by microcavities. One common mechanism for such reflection is Rayleigh backscattering in high-quality-factor microcavities [Fig. 1(a1)] [30], which can be induced by fabrication imperfections and has been employed for self-injection locking laser and microcomb generation [25]. However, a significant challenge with Rayleigh backscattering arises from the inherent randomness in the reflection ratio [14], both among different resonances within identical cavities and among identical resonances in different

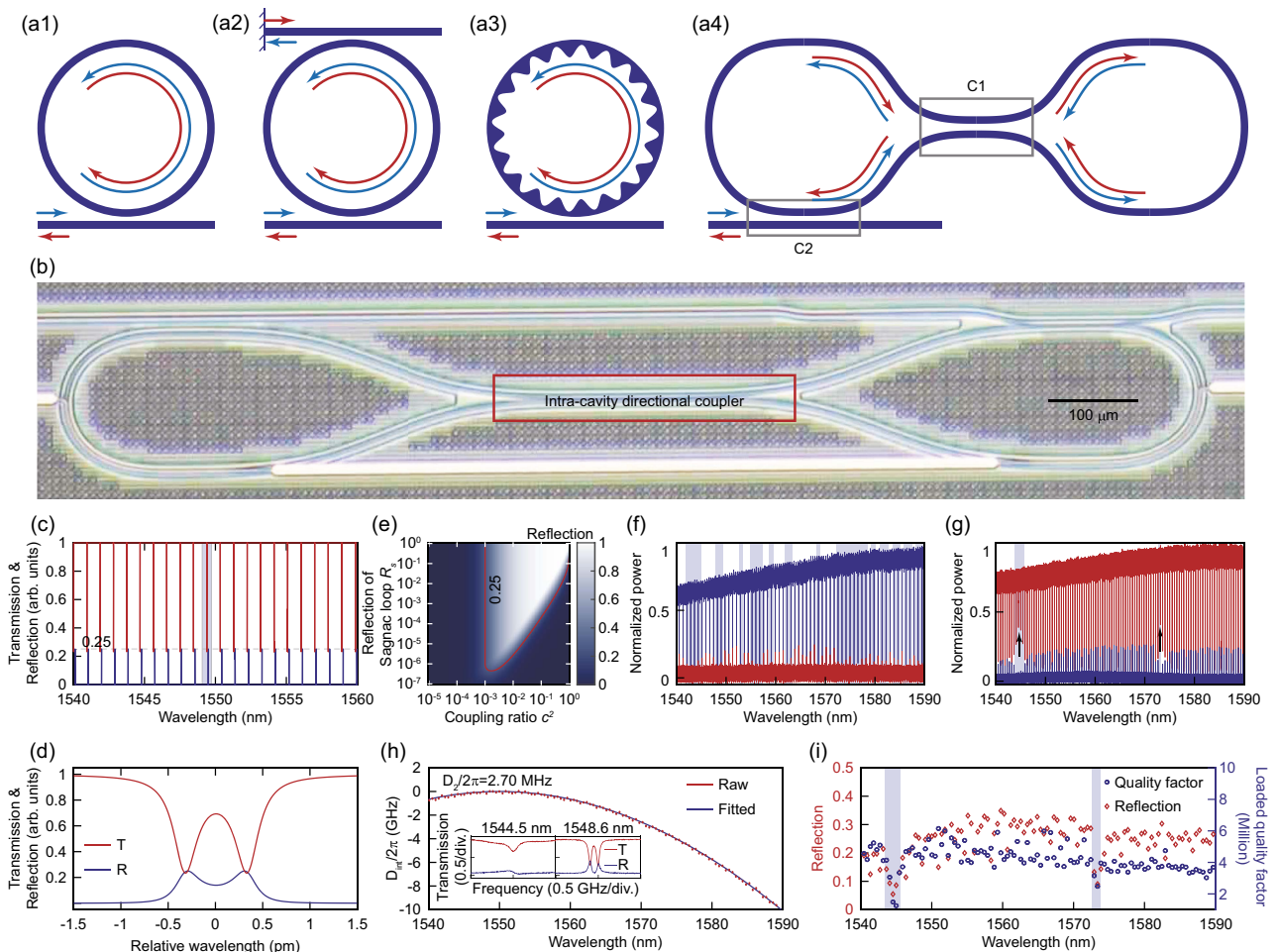


**Fig. 1.** Simulation and experiment results of transmission and reflection. (a) Different schemes of reflection or backscattering for injection locking. (b) The photograph of the Sagnac ring and the ring structure are lighted by green. (c) Simulated transmission (red line) and reflection (blue line) of the Sagnac ring. (d) Simulated transmission (red line) and reflection (blue line) of the resonance around 1550 nm which is shadowed with light blue in (c). (e) Simulated reflection under different intracavity reflection index and coupling index. (f) Tested transmission (red line) and reflection (blue line) of a normal ring resonant. (g) Tested transmission (red line) and reflection (blue line) of a Sagnac ring resonant, the shadowed areas in (f), (g), and (i) mark resonances with relatively low reflection (lower than 0.1). (h) Tested integrated dispersion of the Sagnac ring. The inset shows the resonances at 1544.5 nm and 1548.6 nm, respectively. (i) Extracted peak reflection and loaded quality factor of the Sagnac ring.

chips. This unpredictability raises concerns about the feasibility of mass-producing self-injection locking optical sources based on Rayleigh backscattering. To ensure the reliability of SIL sources, alternative controlled reflection mechanisms have been proposed. One straightforward approach involves incorporating an add-drop microring and placing a reflector at the drop port [Fig. 1(a2)] [31] or coupling the input waveguide with the drop waveguide [32] to induce a robust reflection. However, the additional coupling region can lead to decrease in the quality factor [33]. To balance the loaded quality factor and the reflection ratio for self-injection locking lasers, these works tend to working with loaded quality factors below  $10^6$ , although the intrinsic quality factors could reach  $10^7$ , as demonstrated in silicon nitride (SiN) [32] and silica [34] platforms. The decreased quality factor can hinder the generation of microcombs by SIL under limited power of integrated laser diodes. A photonic crystal ring resonator (PhCR) is the other

promising method [Fig. 1(a3)] that can deterministically introduce backscattering [35]. Self-injection locking laser and microcomb generation have been demonstrated in PhCRs [36]. While effective, the production of these resonators demands a precision fabrication process, with pattern sizes even smaller than 50 nm. Additionally, achieving wide-band reflection with this approach can be challenging. Alternatively, it is possible to induce wide-band reflection by etching a single hole on the microring as a broadband scatterer. However, this also necessitates the fabrication of delicate structures, and localized microcomb generation has not yet been observed with this method [33].

In this study, we present a reliable reflection mechanism achieved by incorporating a Sagnac loop [37,38] into the microcavity as shown in Fig. 1(a4), commonly referred to as a Sagnac ring, as reported in previous works [39,40]. We have developed theoretical models for the Sagnac ring. According to the model, precise control over the reflection ratio can be

attained by adjusting the intracavity coupler and the coupling state. To validate this concept, we have manufactured a Sagnac ring on the SiN platform. Within the wavelength range of 1540 to 1590 nm, consistent reflections are observed for different resonances. Furthermore, by directly coupling the Sagnac ring with a distributed feedback (DFB) laser diode, we have successfully demonstrated the self-injection locking laser, locking to each resonance within the tuning band of the DFB laser diode. Additionally, our simulations have predicted the existence of localized microcombs in a normal-dispersion cavity with broadband forward–backward field coupling. We have observed the localized microcomb generation in an experiment through self-injection locking. This work offers a dependable and practical scheme for advancing self-injection locking technology, opening new possibilities for its application for wafer-scale production.

## 2. PRINCIPLE AND CHARACTERIZATION OF ESSENTIAL PARAMETERS

The proposed Sagnac ring structure is illustrated in Fig. 1(a4), wherein a Sagnac loop is positioned within the cavity rather than at the drop port. The Sagnac loop serves as a prevalent reflector in integrated optical circuits, featuring a waveguide that couples with itself at its central section through a directional coupler denoted as C1. As the optical field traverses the loop, a portion of the light is coupled back, leading to the reflection. The theoretical model for the Sagnac loop has been thoroughly established and well-characterized [37]. In this context, we can describe the coupler using the scatter matrix  $S$ , which is defined as follows:

$$S = \begin{bmatrix} t_s & i\kappa_s \\ i\kappa_s & t_s \end{bmatrix}, \quad (1)$$

where  $t_s$  and  $\kappa_s$  are the transmission and coupling coefficient of the coupler. The transmission  $T_s$  and reflection  $R_s$  of the Sagnac loop can be expressed as

$$\begin{aligned} R_s &= 2i\kappa_s t_s \cdot e^{i\beta L_s} e^{-\alpha L_s}, \\ T_s &= (t_s^2 - \kappa_s^2) \cdot e^{i\beta L_s} e^{-\alpha L_s}, \end{aligned} \quad (2)$$

where  $\beta$  is the propagation constant,  $L_s$  is the length of the loop, and  $\alpha$  is the loss rate of the loop. For the ease of expression, we define  $2\kappa_s t_s$  and  $t_s^2 - \kappa_s^2$  as  $r$  and  $t$ , respectively, which are the forward–backward coupling coefficient and transmission coefficient of the Sagnac loop. Then, we will give the transmission and reflection model of the Sagnac ring. For a simpler format, the two optical lengths from C2 to C1 are assumed as the same, which can be realized by moving the position of C2. The results where the optical lengths are not the same are given in Appendix A. The intracavity field can be expressed as

$$\begin{aligned} f &= \frac{BD - AC}{B^2 - A^2}, \\ b &= \frac{BC - AD}{B^2 - A^2}, \end{aligned} \quad (3)$$

where

$$\begin{aligned} A &= tc \cdot ae^{i\varphi} - 1, \\ B &= r\tau \cdot ae^{i\varphi} \cdot i, \\ C &= tc \cdot ae^{i\varphi} \cdot (-i), \\ D &= rc \cdot ae^{i\varphi}. \end{aligned} \quad (4)$$

$f$  and  $b$  are the intracavity forward and backward field;  $A$ ,  $B$ ,  $C$ , and  $D$  are self-defined parameters;  $a$  is the loss coefficient of single round-trip;  $\tau$  and  $c$  are the transmission coefficient and coupling coefficient of coupler C2; and  $\varphi$  is the phase of the total cavity pass. Based on this model, we can calculate the transmission and reflection of the Sagnac ring. Figure 1(c) shows the calculated transmission and reflection of the Sagnac ring under  $\tau = a$ . It is worth noting that, as we tune  $r$  within a wide range, the reflection is close to but does not exceed 0.25 even as  $r = 1$ . Considering  $r = 1$ ,  $t = 0$ , and  $\tau = a$ , the backward field coupled out the cavity will be

$$b = \frac{cae^{i\varphi}}{-\tau^2 a^2 e^{i2\varphi} + 1}. \quad (5)$$

Under  $\varphi = n\pi$  ( $n \in N$ ), the backward field reaches its maximum, or meets the resonant condition, and

$$b = \frac{1 - 3a^2}{4a^3}. \quad (6)$$

As  $a$  is close to 1 or in a high-quality-factor microring, the reflection  $|b|^2$  will be close to 0.25.

Figure 1(d) shows the spectrum of one resonance around 1550 nm as shadowed in Fig. 1(c). Different from an extracavity reflection as depicted in Fig. 1(a2), the intracavity reflection will also induce resonance splitting, where one resonance splits into two resonances. The splitting frequency mainly depends on the intracavity forward–backward field coupling as demonstrated in Ref. [41]. As the reflection is the most concerned parameter here, we give a map of reflection under different coupling index ( $c^2$ ) and different reflection of the Sagnac loop, as shown in Fig. 1(e), with the round-trip loss  $1 - a^2$  set to 0.001. It is worth noting that under  $\tau = a$ , the reflection reaches around 0.25 whenever  $r$  is larger than  $1 - a$ . For a larger reflection,  $\tau < a$  is necessary with high enough  $r$ .

For the demonstration of the Sagnac ring, we designed and fabricated the Sagnac ring on a SiN platform, as shown in Fig. 1(b). The tested reflection and transmission spectra are depicted in Fig. 1(g). Broadband and consistent reflection is observed with the wavelength range from 1540 nm to 1590 nm. At the short wavelength side, the reflection is decreased which is caused by a lower coupling coefficient between the bus waveguide and the microcavity. The depths of transmission resonances around 1544 nm and 1573 nm are relatively low, resulting from the coupling between the fundamental mode and high-order mode [42]. The reflection at corresponding bands also decreases due to lower quality factors. The extracted integrated dispersion curve is given in Fig. 1(h), showing a typical normal dispersion. Here we only focus on the resonances at the high-frequency (short wavelength) side of the two split resonances. The insets show the resonances affected and unaffected by high-order modes. The extracted reflection and loaded quality factors are given in Fig. 1(i), where the loaded quality factors vary around  $4 \times 10^6$ . By adopting the Sagnac ring, all

resonances within 1540 nm to 1590 nm show a reflection larger than 0.1, and the reflection round 1560 nm could reach 0.3. As a comparison, we also fabricate a racetrack ring with 100 GHz free spectral range (FSR), with the same waveguide structure. The loaded quality factor of the normal cavity is around  $5 \times 10^6$  and the transmission and reflection spectra are given in Fig. 1(f). Due to the random Rayleigh backscattering, the reflection of different resonances fluctuated within a wide range, where some resonances even show neglectable reflection. Compared with the normal all-pass microring, the proposed Sagnac ring provides a reliable reflection without degenerating the quality factor. The reflection is induced by an intracavity directional coupler, which is the common structure for integrated circuits. We believe that the proposed Sagnac ring is attractive for the mass production of self-injection locking sources.

### 3. ROBUST SELF-INJECTION LOCKING LASER FOR DIFFERENT WAVELENGTHS

Contributing to the consistent reflection over a wide operation band, we can achieve SIL lasers for each resonance. In our experimental setup [Fig. 2(a)], we directly couple a DFB laser diode with the Sagnac ring. Both the SiN chip and the laser diode are mounted on separate temperature controllers respectively to stabilize the resonant frequency of the Sagnac ring and the laser cavity. These chips can also be mounted on one temperature controller if packaged or monolithically integrated [14]. Operating at a driving current of 200 mA, the laser diode lases at approximately 1549 nm with an output power of around 15 dBm. By adjusting the temperature of the laser diode within a range of 20°C to 40°C, we can tune the output wavelength from 1547.80 nm to 1550.50 nm under free-running conditions.

As the laser diode is coupled with the SiN chip, the Sagnac ring provides narrow-band reflection to the laser diode at its resonant frequencies. We can finely control the gap between the SiN chip and the laser diode to adjust the feedback phase from the microring to the laser diode, a critical factor in achieving self-injection locking. By changing the temperature of the laser diode to align its output wavelength with the Sagnac ring's resonance and tuning the feedback phase, we can realize SIL lasers. For the measurement of SIL lasers, the output from the SiN chip is coupled through a lensed fiber and split into an optical spectrum analyzer (OSA) and a phase noise testing link, as shown in Fig. 2(b).

Figures 2(c) and 2(d) display the tested phase noise and frequency noise of the SIL lasers, which are locked to different resonances, compared to free-running DFB lasers at 1549.2 nm. Thanks to the self-injection locking process, the phase noise of the hybrid laser is suppressed by more than 30 dB. The frequency noise reaches its lowest point around an offset frequency of approximately 2 MHz, indicating the white noise floor. The measured minimum frequency noises are  $4.57 \text{ Hz}^2/\text{Hz}$ ,  $8.02 \text{ Hz}^2/\text{Hz}$ ,  $3.88 \text{ Hz}^2/\text{Hz}$ ,  $4.37 \text{ Hz}^2/\text{Hz}$ ,  $11.88 \text{ Hz}^2/\text{Hz}$ , and  $9.01 \text{ Hz}^2/\text{Hz}$  for wavelengths of 1547.9 nm, 1548.3 nm, 1548.95 nm, 1549.37 nm, 1549.82 nm, and 1550.46 nm, respectively, indicating a minimum intrinsic linewidth of 24.38 Hz. This is significantly reduced from the 80.78 kHz intrinsic linewidth of the free-running laser. Figure 2(e) presents the measured spectra recorded with a 10 dB offset, considering a 10% split power. Except for the SIL laser at 1550.46 nm, all lasers exhibit power levels greater than 10 dBm.

Notably, thermal phase shifters are positioned above the Sagnac ring and the waveguide between the laser diode and the Sagnac ring. As we have demonstrated SIL lasers for different resonances, this device has the potential to achieve SIL

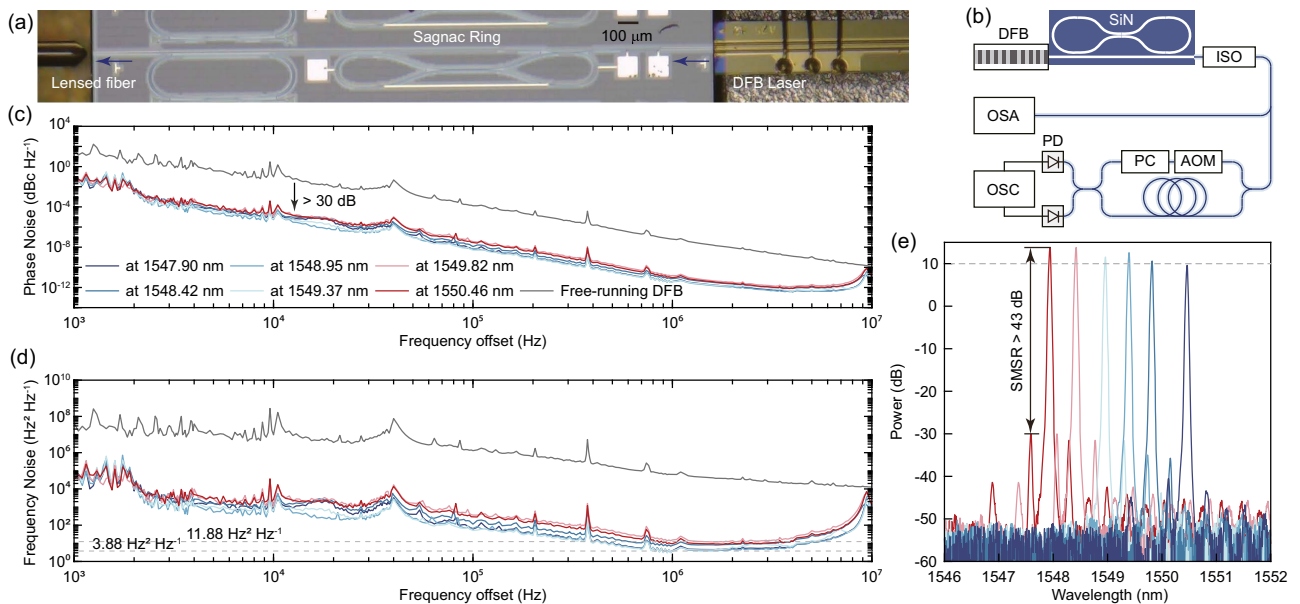


**Fig. 2.** Self-injection lasers employing the Sagnac ring. (a) The photograph of the SIL laser. (b) The setup of the test link for SIL lasers. DFB, distributed feedback laser diode; ISO, optical isolator; OSA, optical spectrum analyzer; AOM, acoustic-optic modulator; PC, polarization controller; PD, photodetector; OSC, oscilloscope. The tested phase noise (c) and frequency noise (d) of SIL lasers locked to different resonances and the free-running DFB laser. (e) Optical spectra of SIL lasers locked to different resonances.

lasers at arbitrary wavelengths by tuning the thermal phase shifter above the Sagnac ring. While our focus was primarily on demonstrating SIL for various wavelengths, we did not extensively fine-tune the working conditions, particularly the feedback phase. This hybrid cavity can be packaged to ensure stable operation and further suppress phase noise at low offset frequencies ( $<10$  kHz) [25]. And superior performance may be attainable by precisely controlling the feedback phase using the thermal phase shifter.

#### 4. COMB GENERATION INDUCED BY FORWARD–BACKWARD FIELD COUPLING

Strong normal dispersion can be witnessed in Fig. 1(h), indicating the absence of spontaneous microcomb generation by sweeping the detuning between the pump laser and the resonance; while as illustrated in Figs. 1(d) and 1(h), the forward–backward field coupling induced by the Sagnac ring will cause resonance splitting. This will lead to localized dispersion changing [40]. As we pump the resonance at the long wavelength (low frequency) side, the pumped mode could undergo effective anomalous dispersion with nearby split resonances at the short wavelength (high frequency) side. This localized anomalous dispersion can support the spontaneous microcomb generation. This phenomenon has been simulated [43] and observed in experiment [40]. Here, different from Ref. [40], the microring is designed for self-injection locking, where the splitting frequency is designed close to the linewidth of the resonance [44], we only observe comb generation of a few comb lines as shown in Fig. 3(b). The corresponding transmission is shown in Fig. 3(a). The laser sweeps into the resonance at the short wavelength side (marked as resonance 1) first, where no comb can be observed. Then the laser will drop into the resonance at the long wavelength side (marked as resonance 2), and the comb state can be observed under a pump power around 15 dBm (before coupling into the cavity). Here we

show the comb generation with comb spacing of eight FSRs around 1555.4 nm, which is far from the resonances influenced by high-order modes.

In simulation, we employ the modified LLE established in Ref. [43]. Using the parameter extracted from the tested data, we could also observe comb generation with spacing of eight FSRs, as shown in Figs. 3(c) and 3(d). With higher pump power, the resonance at the long wavelength side will be covered by the resonance at the short wavelength side due to the nonlinear effects. In the experiment, raising the pump power up to around 23 dBm, we can observe Raman comb generation. We did not observe a localized comb state by sweeping the pump laser. Previous works [40,43] also miss localized states in the Sagnac ring with normal dispersion.

#### 5. EXISTENCE OF LOCALIZED MICROCOMBS

As discussed in the previous part, the localized anomalous dispersion can enable the spontaneous microcomb generation in the normal-dispersion cavity by simply sweeping the resonances from the short wavelength side to the long wavelength side. However, achieving a mode-locked microcomb state has proven to be a challenging process [40,43]. In the case of a cavity where each resonance experiences forward–backward field coupling, which is the condition in the Sagnac ring, the existence of mode-locked states has remained unconfirmed. Utilizing the coupling equation established in Ref. [43], analysis to explore the existence and stability of localized states is conducted. Figure 4(a) illustrates the trajectory of solutions under a specific parameter set. The gray (forward) and brown (backward) lines represent homogeneous steady states (HSS) or continuous wave states, in other words, with solid lines denoting stable solutions and dashed lines indicating unstable ones. Due to intracavity reflection, when light couples into the microcavity, both forward light and backward light exist within the cavity. In contrast to scenarios without forward–backward

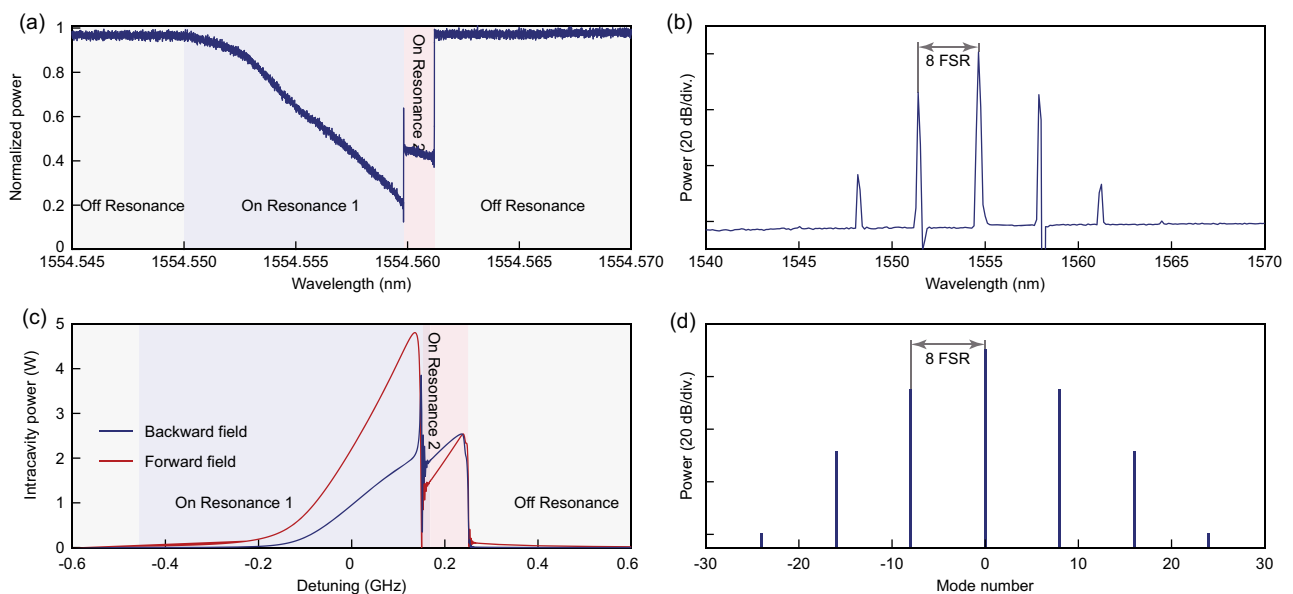


**Fig. 3.** Microcomb generation due to forward–backward field coupling. (a) The transmission of the Sagnac ring of resonances around 1554.5 nm. (b) The generated microcomb. (c) The simulated intracavity power trace as the pump laser sweeping. (d) The simulated microcomb.

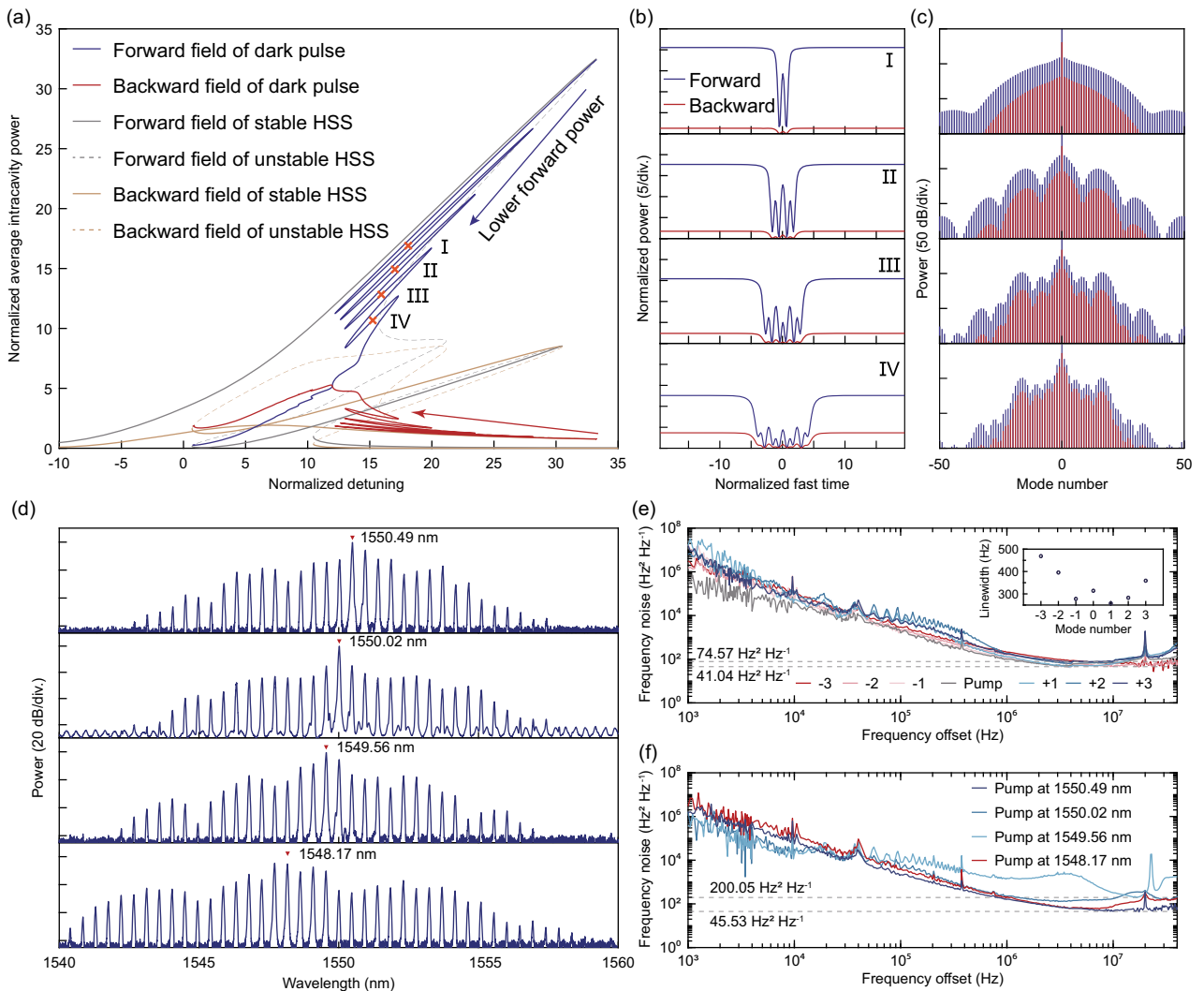


**Fig. 4.** Localized microcomb states in the Sagnac ring. (a) The solution trace in the Sagnac ring with normal dispersion. The single period pulse shapes (b) in time domain and optical spectra (c) of different dark pulse states under conditions marked in (a). (d) Generated localized comb states locked to different resonances. (e) Tested frequency noise curves of different comb lines of the dark pulse locked to the resonance around 1550.49 nm. The inset shows the corresponding intrinsic linewidths. (f) The measured frequency noise curves of  $-2$  comb line of different combs depicted in (d).

coupling, more than three solutions can coexist within the cavity under certain detuning.

Based on previous works [43], we extended our investigation to track the dark pulse solution around the short-wavelength-side resonance using the numerical continuation method. Notably, in our analysis of solutions, we observe that the presence of backward light, with its cross-phase-modulation (XPM) effect on forward light, extends the existence range of the resonant peak compared to that without forward-backward coupling [45]. The trajectory of the dark pulse solution undergoes deformation due to the influence of backward light. As the order of the dark pulse (indicative of the width of the depression) increases, we observed a gradual reduction in the power of forward light, accompanied by an initial increase and subsequent decrease in the power of backward light. In Fig. 4(b), we present the time-domain shapes of the first four orders of dark pulses, where the forward field diminishes gradually while

the backward field strengthens. Notably, the overall shape of the dark pulse in both the time and frequency domains [Fig. 4(c)] remains consistent with that of a normal-dispersion cavity.

Here, we simulate the localized states by self-injection locking in experiment. Figure 4(d) illustrates the various dark pulse combs we observed in the experiment. In contrast to self-injection locking lasers, we set the laser operating current to 300 mA to ensure higher on-chip power, which is critical for the generation of microcombs. Our experimental assessment of injection-locked dark pulses is limited to pump resonances around 1550.49 nm, 1550.02 nm, 1549.56 nm, and 1548.17 nm. Theoretically, localized states exist at other resonances; however, our experimental tests yielded incoherent comb states at resonances around 1548.95 nm and 1548.42 nm. This could be attributed to the possibility that each resonance can achieve self-injection locking, resulting in some overlap between them,

**Table 1. Comparison of Different Schemes of Integrated Self-Injection Locking Lasers**

Platform	Quality Factor ( $\times 10^6$ )	Reflection Origin	Wide-Band SIL Laser	Intrinsic Linewidth (Hz)	Comb Generation
SiN [25]	150	Rayleigh back-scattering		1.2	Y
SiN [31]	0.055	Reflection at drop port	Y	>314	N
SiN [14]	50 <sup>a</sup>	Rayleigh back-scattering		5	Y
SiN [36]	1.6	Photonic crystal	N		Y
SiN [33]	0.8	Hole defect	Y	34.1	N
SiN [47]	0.52	Reflection at drop port	Y	22	N
Silica [34]	0.791	Reflection at drop port	Y	27	N
SiN [48]	0.5	Reflection at drop port	Y	8000	N
SiN [49]	42	Rayleigh back-scattering		3	Y
SiN (this work)	4	Intracavity Sagnac loop	Y	24.38	Y

<sup>a</sup>Intrinsic quality factor.

which in turn makes it challenging to observe the coherent comb state of certain peaks. In Fig. 4(e), we present the frequency noise of seven comb teeth, including the locked pump (marked 0) at 1550.49 nm, as well as the ones on the short wavelength side (marked -3 to -1) and the long wavelength side (marked +1 to +3). Notably, each curve reaches its minimum at a frequency offset around 5 MHz, with values ranging from 41.04 Hz<sup>2</sup>/Hz to 74.57 Hz<sup>2</sup>/Hz. The inset depicts the intrinsic linewidths of the seven comb teeth, revealing a gradual increase trace from the pump to the sides [46]. Figure 4(f) depicts the frequency noise of the -2 comb line of different comb states shown in Fig. 4(d). The observed reduction in frequency noise compared to that of the DFB laser signifies that the optical comb is in the self-injection locked state.

## 6. CONCLUSION

In Table 1, we give a comparison of different schemes for integrated self-injection locking lasers. Compared with the external cavity laser scheme [50–53], the tunable bandwidth of self-injection locking lasers is much shorter, while the coherence of SIL sources [54] is much higher than that of the ECL scheme. Also, the Sagnac ring can be adopted for the external cavity laser scheme. As we claimed before, employing the Sagnac ring, we can induce robust and controlled reflection under a wide operation band, without decreasing the quality factor or involving the fabrication of delicate structures. The proposed scheme is desired for mass-production and widespread applications. The localized microcomb states with broadband forward–backward reflection are first demonstrated in simulation and in experiment, as far as we know. Here, we only present a raw study of such states. It is worth noting that with the changing of the forward–backward coupling strength, the existence range and stability of dark pulses will be changed. This is also interesting and will be illustrated in future works, combining with the analysis in anomalous dispersion cavities. In addition, contributing to the simple structure, the novel concept of robust reflection can be transferred to any integrated photonic platform.

## APPENDIX A: THE MODEL OF THE SAGNAC RING IN A GENERAL CASE

In the main text, we give the model of the Sagnac ring in the case that the two optical paths between C1 and C2 are the

same; while for a general condition, the two paths can be different. Considering the two paths have different lengths  $l_1$  and  $l_2$ , the transmission and reflection can be expressed in a similar form to Eq. (3):

$$f = \frac{BD - AC}{B^2 - A^2},$$

$$b = \frac{BC - AD}{B^2 - A^2} \cdot \exp(-Z \cdot \Delta l), \quad (\text{A1})$$

where  $Z$  is defined as  $-\alpha + i\beta$  and  $\Delta l$  is equal to  $l_2 - l_1$ . Under this condition, there will be a phase difference for backward field. Under the linear model, the transmission and reflection will be the same.

## APPENDIX B: COMPARISON OF ADD-DROP RINGS AND SAGNAC RINGS

To show the advantage of the Sagnac ring over the conventional add-drop ring scheme, we give the simulation results of the reflection and the loaded quality factor of different microcavities, where the free spectral range is 50 GHz, the wavelength is 1550 nm, and the intrinsic quality factor is  $10^7$ . The reflection and the loaded quality factor are the most important factors for self-injection locking lasers and the microcomb generation. For the add-drop ring with the Sagnac loop at the drop port, we assume that the two ring-waveguide couplers have identical parameters and the reflection of the Sagnac loop is 1. In this case, the reflection of the microcavity is determined by the square of the loss from the input to the drop port of the add-drop ring, as the reflected light needs to pass through the add-drop ring twice. For the Sagnac ring, we examine two cases with the reflection ratio  $R$ , of the intracavity Sagnac loop set to 1 and 0.001, respectively. The simulated loaded quality factor and the reflection ratio of the cavity are illustrated in Fig. 5. Due to the additional coupler, the loaded quality factor of the add-drop ring is lower than that of the Sagnac ring under the same reflection. The lower quality factor will degenerate the linewidth enhancement for self-injection locking lasers and increase the required pump power for localized microcomb generation. Regarding the robustness and complexity, the Sagnac ring does not involve any additional complex component compared with add-drop rings. The primary challenge associated with the Sagnac ring lies in the complex design process required for the suppression of high-order modes.

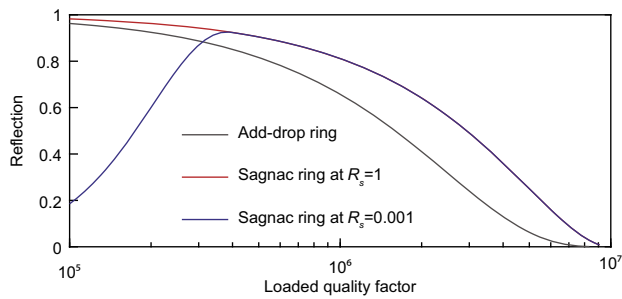


**Fig. 5.** Comparison of Sagnac rings and add-drop rings with Sagnac loops at the drop port.

### APPENDIX C: DETAILED PARAMETERS OF THE CHIPS

As shown in Fig. 6(a), the Sagnac ring consists of two partial Euler bends (red lines), four S-shape bends (blue lines), and two straight waveguides (yellow lines). The minimum bend radius of the partial Euler bend is  $55\ \mu\text{m}$ . The offset in the  $x$  direction and  $y$  direction of the S-shape bends is  $450\ \mu\text{m}$  and  $72.5\ \mu\text{m}$ , respectively. The length of the straight waveguides is  $100\ \mu\text{m}$ . The gap of the coupler C1 is  $2\ \mu\text{m}$ . The Sagnac ring is coupled with a bus waveguide at the connection (C2) of the partial Euler bend and the S-shape bend. The gap of the coupler C2 is  $0.8\ \mu\text{m}$ . The entire ring consists of the rectangular waveguide with the width and the height of  $3\ \mu\text{m}$  and  $0.3\ \mu\text{m}$ , respectively. The wide waveguide can decrease the propagation loss to increase the quality factor. For assessing the propagation loss of the waveguide, we designed and fabricated seven racetrack microcavities of  $100\ \text{GHz}$  FSR with the same parameters on seven different chips. The histogram of estimated loaded quality factors of the seven racetrack microcavities around  $1550\ \text{nm}$  is given in Fig. 6(b). The average and the standard deviation of the loaded quality factors are  $5.52 \times 10^6$  and  $2.47 \times 10^6$ . We also measure seven Sagnac rings with the same design used in this work. The histogram of estimated loaded

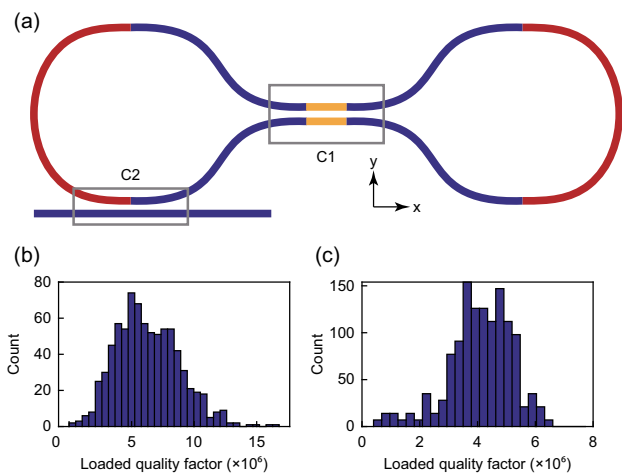


**Fig. 6.** Parameter of the Sagnac ring. (a) The structure of the Sagnac ring. (b) The histogram of estimated loaded quality factors of racetrack rings. (c) The histogram of estimated loaded quality factors of Sagnac rings.

quality factors is shown in Fig. 6(c), where the average and the standard deviation of the loaded quality factors are  $4.13 \times 10^6$  and  $1.16 \times 10^6$ . The threshold current of the DFB laser diode is  $10\ \text{mA}$ . The output power of the DFB laser diode reaches  $18\ \text{dBm}$  under the driving current of  $350\ \text{mA}$ , with the diode voltage of  $1.4\ \text{V}$ . The edge coupler of the SiN chip consists of a  $220\ \mu\text{m}$ -long inverse taper with the waveguide width widening from  $0.28\ \mu\text{m}$  to  $1\ \mu\text{m}$ . The output power collected with a lensed fiber through the SiN chip is  $13\text{--}14\ \text{dBm}$ , indicating a total insertion loss of  $4\text{--}5\ \text{dB}$ .

### APPENDIX D: THE SELF-INJECTION LOCKING RANGE

In addition to the linewidth measurement of the SIL laser, we also give a measurement of the self-injection locking range, by sweeping the driving current of the laser diode. The output of the hybrid laser is beat with a reference laser in a photodetector, and the beating signal is recorded by an oscilloscope for offline process, as depicted in Fig. 7(a). Figure 7(b) shows the time-frequency spectrogram of the beating signal when the DFB laser cavity frequency or the free-running laser frequency is swept by tuning the driving current. Under the free-running state, the laser frequency is chirped with the driving current, while under the self-injection locking state, the laser frequency is locked by the SiN microcavity and changed slowly with the current sweep. In the experiment, we find the locking range of the hybrid laser is  $9\ \text{GHz}$  for both forward and backward detuning, close to the locking range ( $13.3\ \text{GHz}$ ) reported in Ref. [28].

### APPENDIX E: THE DELAYED SELF-HETERODYNE METHOD FOR THE LINEWIDTH MEASUREMENT

Here we adopt the delayed self-heterodyne method for the linewidth measurement. The experimental setup, illustrated in

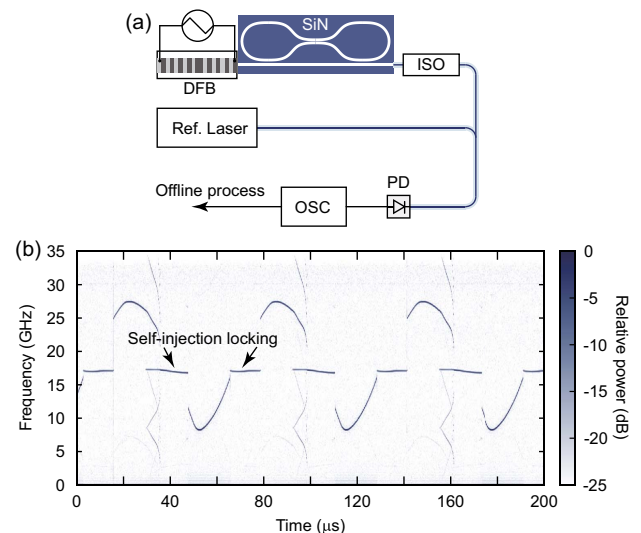


**Fig. 7.** (a) The experiment setup of the measurement. DFB, distributed feedback laser diode; ISO, optical isolator; Ref. Laser, reference laser; PD, photodetector; OSC, oscilloscope. (b) The beat note spectrum of the hybrid laser with a reference laser during the driving current sweep of the DFB laser.



Fig. 2(b), includes a Mach–Zehnder interferometer, a polarization controller, an acoustic-optic modulator, and a 5 km fiber. The beating signal is recorded by a real-time oscilloscope. The double-sideband power spectral density  $S_{\Delta\varphi}(f)$  of the delayed laser phase  $[\Delta\varphi = \varphi(t) - \varphi(t - \tau)]$  noise can be extracted from the recorded data, where  $\tau$  represents the time delay between the two arms of the Mach–Zehnder interferometer. The laser frequency noise can be determined as

$$S_v(f) = \frac{f^2}{4[\sin(\pi f \tau)]^2} S_{\Delta\varphi}(f). \quad (\text{E1})$$

The measured frequency noises are given in Fig. 2(d) and Figs. 4(e) and 4(f). At high offset frequencies, the white frequency noise, also known as quantum noise, is the dominate noise, which determines the intrinsic linewidth. The intrinsic linewidth can be estimated by multiplying the white noise level by  $2\pi$ . Further details of the process are available in Ref. [55].

## APPENDIX F: SIMULATION OF COMB STATES IN THE SAGNAC RING

For the simulation of comb states, coupled Lugiato–Lefever-type equations are used:

$$\begin{aligned} t_R \frac{\partial F(t, \tau)}{\partial t} &= \left[ -\left( \frac{\kappa + \theta}{2} - i\delta_0 \right) + iL \frac{\beta_2}{2} \frac{\partial^2}{\partial \tau^2} \right] \cdot F \\ &+ ig \cdot B(-\tau) + iL\gamma(|F|^2 + 2P_B)F + \sqrt{\theta}F_{\text{in}}, \\ t_R \frac{\partial B(t, \tau)}{\partial t} &= \left[ -\left( \frac{\kappa + \theta}{2} - i\delta_0 \right) + iL \frac{\beta_2}{2} \frac{\partial^2}{\partial \tau^2} \right] \cdot B \\ &+ ig^* \cdot F(-\tau) + iL\gamma(|B|^2 + 2P_F)B, \end{aligned} \quad (\text{F1})$$

where  $t_R$  and  $L$  are the round-trip time and length,  $\kappa$  is the single-pass loss rate,  $\delta_0$  is the detuning,  $\theta$  is the coupling index,  $\beta_2$  is the second-order dispersion,  $g$  is the coupling rate between forward and backward fields,  $P_F$  and  $P_B$  are the average powers of forward and backward fields, and  $F$  and  $B$  are the forward and backward fields. For the simulation of Fig. 3, the intracavity fields is initialized with noise background and the detuning  $\delta_0$  is swept for the comb generation.  $t_R$  and  $L$  are set to 17.88 ps and 2.40 mm, respectively, considering the FSR of 55.93 GHz.  $\beta_2$  is set to  $1134.66 \text{ ps}^2 \text{ km}^{-1}$ .  $\kappa$  and  $\theta$  are equal to 0.0027 as  $Q_i = Q_c = 8 \times 10^6$ .  $\gamma$  is equal to  $1 \text{ m}^{-1} \text{ W}^{-1}$  and  $g$  is  $3.2\kappa$ . The pump power is set to 28 mW. For the simulation in Fig. 4, due to the comb states not being able to be stimulated by simply sweeping the detuning, the pulse pump condition is first used to stimulate the dark pulse state. The generated dark pulse state is used as the guess solution for the numerical continuation method for the track of existing dark pulse solutions. Also, the pump power is set to 50 mW.

**Funding.** National Key Research and Development Program of China (2021YFB2800400); National Natural Science Foundation of China (12204021, 62105008, 62235002, 62235003, 62322501, 8200908114); Beijing Municipal Science and Technology Commission (Z221100006722003); Natural Science Foundation of Beijing Municipality (Z210004); Nantong Municipal

Science and Technology Bureau (JB2022008, JC22022050); China Postdoctoral Science Foundation (2021T140004).

**Acknowledgment.** The authors thank Dan Sun, Hao Wu, and Lingwei Meng in Peking University Yangtze Delta Institute of Optoelectronics for equipment support.

**Disclosures.** The authors declare no conflicts of interest.

**Data Availability.** The data that support the findings of this study are available from the corresponding authors upon reasonable request.

## REFERENCES

- K. Kikuchi, "Fundamentals of coherent optical fiber communications," *J. Lightwave Technol.* **34**, 157–179 (2015).
- S. L. Olsson, J. Cho, S. Chandrasekhar, *et al.*, "Probabilistically shaped PDM 4096-QAM transmission over up to 200 km of fiber using standard intradyne detection," *Opt. Express* **26**, 4522–4530 (2018).
- D. Marpaung, J. Yao, and J. Capmany, "Integrated microwave photonics," *Nat. Photonics* **13**, 80–90 (2019).
- J. Yao and J. Capmany, "Microwave photonics," *Sci. China Inf. Sci.* **65**, 221401 (2022).
- Z. Tao, Y. Tao, M. Jin, *et al.*, "Highly reconfigurable silicon integrated microwave photonic filter towards next-generation wireless communication," *Photonics Res.* **11**, 682–694 (2023).
- Z. L. Newman, V. Maurice, T. Drake, *et al.*, "Architecture for the photonic integration of an optical atomic clock," *Optica* **6**, 680–685 (2019).
- W. Loh, J. Stuart, D. Reens, *et al.*, "Operation of an optical atomic clock with a Brillouin laser subsystem," *Nature* **588**, 244–249 (2020).
- G. Lihachev, J. Riemensberger, W. Weng, *et al.*, "Low-noise frequency-agile photonic integrated lasers for coherent ranging," *Nat. Commun.* **13**, 3522 (2022).
- R. Chen, H. Shu, B. Shen, *et al.*, "Breaking the temporal and frequency congestion of lidar by parallel chaos," *Nat. Photonics* **17**, 306–314 (2023).
- Y.-H. Lai, M.-G. Suh, Y.-K. Lu, *et al.*, "Earth rotation measured by a chip-scale ring laser gyroscope," *Nat. Photonics* **14**, 345–349 (2020).
- M.-G. Suh, Q.-F. Yang, K. Y. Yang, *et al.*, "Microresonator soliton dual-comb spectroscopy," *Science* **354**, 600–603 (2016).
- B. Dahmani, L. Hollberg, and R. Drullinger, "Frequency stabilization of semiconductor lasers by resonant optical feedback," *Opt. Lett.* **12**, 876–878 (1987).
- W. Liang, V. Ilchenko, D. Eliyahu, *et al.*, "Ultralow noise miniature external cavity semiconductor laser," *Nat. Commun.* **6**, 7371 (2015).
- C. Xiang, W. Jin, O. Terra, *et al.*, "3D integration enables ultralow-noise isolator-free lasers in silicon photonics," *Nature* **620**, 78–85 (2023).
- Z. Ye, H. Jia, Z. Huang, *et al.*, "Foundry manufacturing of tight-confinement, dispersion-engineered, ultralow-loss silicon nitride photonic integrated circuits," *Photonics Res.* **11**, 558–568 (2023).
- M. W. Puckett, K. Liu, N. Chauhan, *et al.*, "422 million intrinsic quality factor planar integrated all-waveguide resonator with sub-MHz linewidth," *Nat. Commun.* **12**, 934 (2021).
- M. A. Tran, C. Zhang, T. J. Morin, *et al.*, "Extending the spectrum of fully integrated photonics to submicrometre wavelengths," *Nature* **610**, 54–60 (2022).
- C. Xiang, J. Liu, J. Guo, *et al.*, "Laser soliton microcombs heterogeneously integrated on silicon," *Science* **373**, 99–103 (2021).
- H. Shu, L. Chang, Y. Tao, *et al.*, "Microcomb-driven silicon photonic systems," *Nature* **605**, 457–463 (2022).
- J. Liu, G. Huang, R. N. Wang, *et al.*, "High-yield, wafer-scale fabrication of ultralow-loss, dispersion-engineered silicon nitride photonic circuits," *Nat. Commun.* **12**, 2236 (2021).
- A. E. Shitikov, I. I. Lykov, O. V. Benderov, *et al.*, "Optimization of laser stabilization via self-injection locking to a whispering-gallery-mode microresonator: experimental study," *Opt. Express* **31**, 313–327 (2023).

22. R. R. Galiev, N. M. Kondratiev, V. E. Lobanov, *et al.*, "Mirror-assisted self-injection locking of a laser to a whispering-gallery-mode microresonator," *Phys. Rev. Appl.* **16**, 064043 (2021).
23. Q. Su, F. Wei, C. Chen, *et al.*, "A self-injection locked laser based on high-Q micro-ring resonator with adjustable feedback," *J. Lightwave Technol.* **41**, 6756–6763 (2023).
24. N. Kondratiev, V. Lobanov, A. Cherenkov, *et al.*, "Self-injection locking of a laser diode to a high-Q WGM microresonator," *Opt. Express* **25**, 28167–28178 (2017).
25. W. Jin, Q.-F. Yang, L. Chang, *et al.*, "Hertz-linewidth semiconductor lasers using CMOS-ready ultra-high-Q microresonators," *Nat. Photonics* **15**, 346–353 (2021).
26. B. Shen, L. Chang, J. Liu, *et al.*, "Integrated turnkey soliton microcombs," *Nature* **582**, 365–369 (2020).
27. A. S. Voloshin, N. M. Kondratiev, G. V. Lihachev, *et al.*, "Dynamics of soliton self-injection locking in optical microresonators," *Nat. Commun.* **12**, 235 (2021).
28. G. Lihachev, W. Weng, J. Liu, *et al.*, "Platicon microcomb generation using laser self-injection locking," *Nat. Commun.* **13**, 1771 (2022).
29. H. Wang, B. Shen, Y. Yu, *et al.*, "Self-regulating soliton switching waves in microresonators," *Phys. Rev. A* **106**, 053508 (2022).
30. M. L. Gorodetsky, A. D. Pryamikov, and V. S. Ilchenko, "Rayleigh scattering in high-Q microspheres," *J. Opt. Soc. Am. B* **17**, 1051–1057 (2000).
31. M. Corato-Zanarella, A. Gil-Molina, X. Ji, *et al.*, "Widely tunable and narrow-linewidth chip-scale lasers from near-ultraviolet to near-infrared wavelengths," *Nat. Photonics* **17**, 157–164 (2023).
32. L. Tang, H. Jia, S. Shao, *et al.*, "Hybrid integrated low-noise linear chirp frequency-modulated continuous-wave laser source based on self-injection to an external cavity," *Photonics Res.* **9**, 1948–1957 (2021).
33. J. Li, B. Zhang, S. Yang, *et al.*, "Robust hybrid laser linewidth reduction using Si<sub>3</sub>N<sub>4</sub>-based subwavelength hole defect assisted microring reflector," *Photonics Res.* **9**, 558–566 (2021).
34. G. Zhang, Q. Cen, T. Hao, *et al.*, "Self-injection locked silica external cavity narrow linewidth laser," *J. Lightwave Technol.* **41**, 2474–2483 (2023).
35. A. Arbabi, Y. M. Kang, C.-Y. Lu, *et al.*, "Realization of a narrowband single wavelength microring mirror," *Appl. Phys. Lett.* **99**, 091105 (2011).
36. A. E. Ulanov, T. Wildi, N. G. Pavlov, *et al.*, "Synthetic reflection self-injection-locked microcombs," *Nat. Photonics* **18**, 294–299 (2024).
37. H. Arianfard, S. Juodkazis, D. J. Moss, *et al.*, "Sagnac interference in integrated photonics," *Appl. Phys. Rev.* **10**, 011309 (2023).
38. X. Jiang, J. Wang, C. Gao, *et al.*, "All-optical NRZ wavelength conversion using a Sagnac loop with optimized SOA characteristics," *J. Semicond.* **36**, 014013 (2015).
39. C. Vázquez, S. E. Vargas, and J. M. S. Pena, "Sagnac loop in ring resonators for tunable optical filters," *J. Lightwave Technol.* **23**, 2555–2567 (2005).
40. J. Zang, S.-P. Yu, D. R. Carlson, *et al.*, "Kerr comb generation in normal-dispersion, bi-directionally coupled microresonators," in *Conference on Lasers and Electro-Optics (CLEO)*, (IEEE, 2023), pp. 1–2.
41. T. Kippenberg, S. Spillane, and K. Vahala, "Modal coupling in traveling-wave resonators," *Opt. Lett.* **27**, 1669–1671 (2002).
42. X. Ji, J. Liu, J. He, *et al.*, "Compact, spatial-mode-interaction-free, ultralow-loss, nonlinear photonic integrated circuits," *Commun. Phys.* **5**, 84 (2022).
43. N. M. Kondratiev and V. E. Lobanov, "Modulational instability and frequency combs in whispering-gallery-mode microresonators with backscattering," *Phys. Rev. A* **101**, 013816 (2020).
44. R. R. Galiev, N. M. Kondratiev, V. E. Lobanov, *et al.*, "Optimization of laser stabilization via self-injection locking to a whispering-gallery-mode microresonator," *Phys. Rev. Appl.* **14**, 014036 (2020).
45. P. Parra-Rivas, E. Knobloch, D. Gomila, *et al.*, "Dark solitons in the Lugiato-Lefever equation with normal dispersion," *Phys. Rev. A* **93**, 063839 (2016).
46. F. Lei, Z. Ye, Ó. B. Helgason, *et al.*, "Optical linewidth of soliton microcombs," *Nat. Commun.* **13**, 3161 (2022).
47. L. Tang, L. Li, J. Li, *et al.*, "Hybrid integrated ultralow-linewidth and fast-chirped laser for FMCW lidar," *Opt. Express* **30**, 30420–30429 (2022).
48. Y. Li, Y. Zhang, H. Chen, *et al.*, "Tunable self-injected Fabry–Perot laser diode coupled to an external high-Q Si<sub>3</sub>N<sub>4</sub>/SiO<sub>2</sub> microring resonator," *J. Lightwave Technol.* **36**, 3269–3274 (2018).
49. C. Xiang, J. Guo, W. Jin, *et al.*, "High-performance lasers for fully integrated silicon nitride photonics," *Nat. Commun.* **12**, 6650 (2021).
50. Y. Fan, A. van Rees, P. J. Van der Slot, *et al.*, "Hybrid integrated InP-Si<sub>3</sub>N<sub>4</sub> diode laser with a 40-Hz intrinsic linewidth," *Opt. Express* **28**, 21713–21728 (2020).
51. Y. Fan, R. M. Oldenbeuving, C. G. Roeloffzen, *et al.*, "290 Hz intrinsic linewidth from an integrated optical chip-based widely tunable InP-Si<sub>3</sub>N<sub>4</sub> hybrid laser," in *Conference on Lasers and Electro-Optics (CLEO)* (IEEE, 2017), pp. 1–2.
52. B. Stern, X. Ji, A. Dutt, *et al.*, "Compact narrow-linewidth integrated laser based on a low-loss silicon nitride ring resonator," *Opt. Lett.* **42**, 4541–4544 (2017).
53. B. Stern, X. Ji, Y. Okawachi, *et al.*, "Battery-operated integrated frequency comb generator," *Nature* **562**, 401–405 (2018).
54. C. Xiang, W. Jin, and J. E. Bowers, "Silicon nitride passive and active photonic integrated circuits: trends and prospects," *Photonics Res.* **10**, A82–A96 (2022).
55. H. Wang, L. Wu, Z. Yuan, *et al.*, "Towards milli-hertz laser frequency noise on a chip," in *Conference on Lasers and Electro-Optics (CLEO)* (IEEE, 2020), pp. 1–2.